International Journal of Microwave and Wireless Technologies, 2013, 5(3), 409–417.
doi:10.1017/S1759078713000329

RESEARCH PAPER

Position estimation of lap joints for seam tracking applications at mm-wave frequencies

JOCHEN O. SCHRATTENECKER[1], ANDREAS HADERER[1], GÜNTHER REINTHALER[2] AND ANDREAS STELZER[1]

In this paper, we present the results of using a frequency-stepped continuous-wave radar system to estimate the position of overlapping and electrically good conductive plates. We especially focus on polarimetric scattering effects caused by the step of a lap joint, which is a common welding-geometry. To model the step's contribution to the overall scattered signal, we use a two-dimensional combined field integral equation (CFIE) approach. For demonstrating its practical applicability, the implemented scattering model is verified by measurements. To emphasize the improvements of position estimation by using a CFIE approach, the outcomes of the model are compared to a commonly used point scattering model. Finally, the numerical signal is utilized to precisely estimate the position of the lap joint.

Keywords: Microwave mesurements, Radar applications

Received 25 October 2012; Revised 13 March 2013; first published online 23 April 2013

I. INTRODUCTION

In automated welding applications the exact position of the welding-geometry is required. Therefore, the aim is to detect unexpected variations in the position of the welding-geometry and consequently enhance the quality of the welding process. Typically, this task is accomplished using optical sensors. Unfortunately, these sensors are very expensive and they are sensitive to environmental stress, caused by fume, dust, and pollution. In contrast, radar sensors are hardly affected by the aforementioned influences.

In this contribution we used mm-wave radars for estimating the position of the welding-geometry's edges. In this paper, we use lap joint geometries with various step thicknesses made out of aluminum, as depicted in Fig. 1. In this work, the capabilities for precise position estimation are explored and additionally the main difficulties of the concept are addressed.

The idea is to use local polarimetric effects, which occur at spatial discontinuities in perfect conducting surfaces, as for instance, at edges or, in our case, at the step of a lap joint geometry. Michaeli [1] already characterized these effects for wedge geometries and presented an equivalent current model to describe their scattering behavior. In the first attempt, we used a point scatterer for position estimation, since the influence of polarimetric scattering is limited to the vicinity of the step. Unfortunately, it turned out that the point model does not provide the required accuracy for precise position estimation. Therefore, a better approach than the point scatterer has to be used. Different methods such as geometrical optics or physical optics [2] represent approximate forms of the scattering behavior of a target. In our case, a more accurate expression, which can additionally describe diffraction effects, is desired. Non-approximate forms are for example integral equation (IE) methods. The incident field on the target geometry induces a current density which is responsible for the scattering behavior. IE techniques cast the solution for the induced current density in the form of an integral. The unknown current density, which is a sum of the physical optics current density and a fringe wave current density [3, 4], is part of the integral. Numerical techniques such as the method of moments (MoM) can be used to solve the current density. The MoM was first introduced by Harrington in 1967 [5]. The link between the scattered field and the surface current density is called impedance matrix and depends on the shape of the target geometry and the calculated frequency only. Calculations of an IE method such as the electric field integral equation (EFIE) or magnetic field integral equation (MFIE) lead to huge equation systems. Thus, even small scaled three-dimensional objects, with expansions of a few wavelengths, can cause high memory costs and long calculation times. For this reason approximation techniques for the IE methods, such as the fast multipole method (FMM), developed by Rokhlin in 1990 [6] or hybrid approaches, as

[1]Institute for Communications Engineering and RF-Systems, Altenberger Str. 69, A-4040 Linz, Austria. Phone : +43 732 2468 6390
[2]Fronius International GmbH, Günter Fronius Str. 1, A-4600 Wels-Thalheim, Austria
Corresponding author:
J. Schrattenecker
Email: j.schrattenecker@nthfs.jku.at

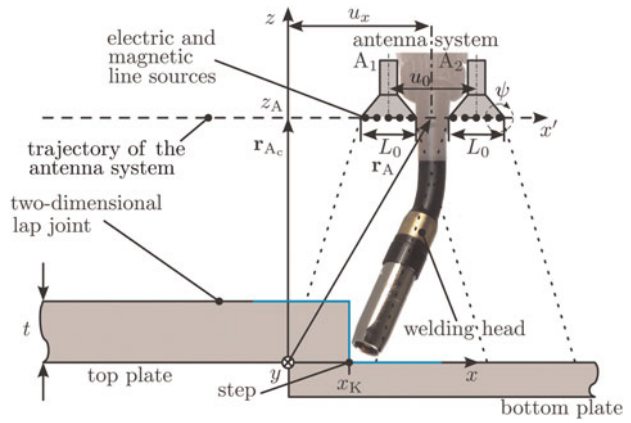

Fig. 1. The pictured two-dimensional geometry is used to describe the simulation model and the measurement setup.

described by Bouché [7], can be used. Another way of reducing the computational and memory effort is to reduce the geometry to two dimensions and calculate the scattering parameter at only one frequency, which was done in this paper. Therefore, we have to check if a model based on these assumptions is precise enough to describe the scattering behavior of the geometry.

To calculate the scattering behavior of the lap joint, we used a combined field integral equation (CFIE) [8, 9] approach, which is a linear combination of the EFIE and MFIE. To verify the models based on the CFIE and a point scatterer, we conducted measurements using a frequency-stepped continuous-wave (FSCW) radar, operating at a center frequency of 27.5 GHz. The FSCW system is built up by a vector network analyzer (VNA) and two pyramidal horn antennas, which are arranged to cover orthogonal polarization planes.

The paper is organized as follows. First, we introduce the system's geometry, being used for the description of the scattering properties and for conducting measurement. Based on this, Section III describes the modeling of the scattering parameters of the lap joint with respect to the position x_K, the step height t, and the position of the radar system $\boldsymbol{r}_A$. In Section IV, the modeled scattering behavior is validated with different measurements. Finally, Section V gives a possible signal processing approach based on CFIE calculations to estimate the position of the lap joint. In addition, position estimation results for measurement scenarios with different step heights t are presented.

II. MEASUREMENT SCENARIO

A) Geometrical description

A schematic diagram of our measurement scenario is depicted in Fig. 1. The welding head, that is part of the system in industrial applications, is in addition shown in the figure, but was not placed in the measurements. It is assumed that the plates are perfectly conducting. This is a reasonable assumption for metals such as aluminum or steel. The upper border of the bottom plate is located in the xy-plane at $z = 0$, and the upper face of the top plate is located at $z = t$. The step, at position x_K, is aligned with the y-axis. At first it is assumed that the plates of the lap joint are large compared to the extension of the antenna footprints in the plane of the objects. Hence, only a single, straight step is illuminated by the antenna system and all other edges can be neglected. The position x_K of the step is the primary point of interest. To gain spatial resolution the concept of a synthetic aperture radar (SAR) is used. The SAR principle requires a relative movement between the radar and the targets. This movement can cause long measurement times. This disadvantage can be overcome by replacing the synthetic aperture by an array of transmitting and receiving elements in future investigations. The antenna array requires a calibration in amplitude and phase among all array elements. This is because the SAR uses a single antenna system and no calibration has to be accomplished. The position of the antenna system's center is described by the vector $\boldsymbol{r}_A(u_x) = [u_x, 0, z_A]^T$, where u_x specifies the radar's location along the one-dimensional aperture and z_A denotes the height of the antenna system. The vector $\boldsymbol{r}_{A_c} = [0, 0, z_A]^T$ refers to the center of the synthetic aperture.

B) Concept overview

The antennas A_1 and A_2 depicted in Fig. 1 form the antenna system of the measurement scenario. For calculation of the CFIE-based model, the antenna system is placed at a position along the synthetic aperture. Subsequently the incident fields on the geometry, caused by the antennas are calculated. The CFIE technique gives us the induced current densities along the geometry by using the MoM. This calculation is performed for a single frequency. The current densities and the incident fields are used to calculate the scattering parameters (see Section III) for the actual aperture position. The computation of the scattering parameters is important to compare the CFIE approach with measurement data. After that the antenna system is moved to the next aperture position and the calculation is repeated. For the simulation and the measurement an equidistant aperture grid is used. The calculated impedance matrix depends on the shape of the geometry and the frequency only. Hence, there is no need to calculate it for every possible aperture point again, since the geometry and the frequency remain unchanged. Only the new incident fields are required to recalculate the surface current density for the next position.

III. NUMERICAL MODEL

The model is split into two different parts. The first one deals with the field source, namely the antenna system. The second part focuses on the scattering behavior of the target, especially the polarimetric effects caused by the step. To minimize the computational costs, the three-dimensional problem is reduced to two dimensions. This is made possible by assuming that the geometry along the y-axis remains unchanged. In addition, the scattering behavior of the lap joint is calculated at the center frequency of the FSCW radar system (27.5 GHz) only. Both constraints make the computed data manageable for real-time applications in digital signal processors.

A) Antenna model

The antenna system is built up by two pyramidal horn antennas [10]. These antennas are radiating a linearly polarized

https://doi.org/10.1017/S1759078713000329 Published online by Cambridge University Press

field, which is important to cover orthogonal polarization planes and detect polarimetric effects caused by the lap joint. In addition, linear polarization is important to isolate different polarized signals directly in the measurements.

For the evaluation a two-dimensional model of the field source is required. In the simulator, the radiation characteristics of the horn antennas are reproduced by electric and magnetic line currents placed in the aperture L_o. The use of both line currents gives the possibility to rotate the polarization of the transmitted field with respect to the step's orientation. For the entire calculation the line currents are aligned with the y-axis. Hence, $\boldsymbol{I}_e = [0, I_{e,y}, 0]^T$ and $\boldsymbol{I}_m = [0, I_{m,y}, 0]^T$ are directed in the y-direction. The two-dimensional radiation patterns are adapted to coincide with those of the horn antennas in the xz-plane. The electromagnetic field of a single electric line source element can be calculated by

$$E_y = -I_{e,y}\frac{\omega_c \mu}{4} H_0^{(2)}(k_c R), \quad H_\Psi = -jI_{e,y}\frac{k_c}{4} H_1^{(2)}(k_c R) \quad (1)$$

and

$$E_\Psi = jI_{m,y}\frac{k_c}{4} H_1^{(2)}(k_c R), \quad H_y = -I_{m,y}\frac{\omega_c \varepsilon}{4} H_0^{(2)}(k_c R) \quad (2)$$

for a single magnetic line source [2]. The circumferential angle around the sources is denoted by Ψ, $\omega_c = 2\pi f_c$ specifies the angular frequency, $k_c = 2\pi f_c / c_0$ denotes the wavenumber at the center frequency, μ stands for the permeability, and ϵ for the permittivity of the medium. The distance between the line source and the point of observation is termed R. The functions $H_0^{(2)}$ and $H_1^{(2)}$ refer to the Hankel function of the second kind of order zero and one, respectively. The incident field emitted by the two-dimensional antenna is given by a superposition of N_a line current elements (In our simulations we chose $N_a = 12$.). This yields to

$$E_y = \sum_{i=0}^{Na-1} -I_{e,y}\frac{\omega_c \mu}{4} \cos\left(\frac{i - \frac{N_a - 1}{2}}{N_a}\pi\right) e^{-j\phi_i} H_0^{(2)}(k_c R_i), \quad (3)$$

$$H_\Psi = \sum_{i=0}^{Na-1} -jI_{e,y}\frac{k_c}{4} \cos\left(\frac{i - \frac{N_a - 1}{2}}{N_a}\pi\right) e^{-j\phi_i} H_1^{(2)}(k_c R_i), \quad (4)$$

for the electric and

$$E_\Psi = \sum_{i=0}^{Na-1} jI_{m,y}\frac{k_c}{4} \cos\left(\frac{i - \frac{N_a - 1}{2}}{N_a}\pi\right) e^{-j\phi_i} H_1^{(2)}(k_c R_i), \quad (5)$$

$$H_y = \sum_{i=0}^{Na-1} -jI_{m,y}\frac{\omega_c \epsilon}{4} \cos\left(\frac{i - \frac{N_a - 1}{2}}{N_a}\pi\right) e^{-j\phi_i} H_0^{(2)}(k_c R_i), \quad (6)$$

for the magnetic line currents placed in the antenna aperture. With the variation of the electric and magnetic line current amplitudes $I_{e,y} = I_o \sin(\varphi_{A_v})$ and $I_{m,y} = I_o\sqrt{\mu/\varepsilon}\cos(\varphi_{A_v})$ the polarization of the two-dimensional antennas, can be rotated around the z-axis. The variable φ_{A_v} is the angle of rotation of the vth antenna. The variable φ_i refers to a phase variation, which depends on geometrical dimensions of the horn antenna and the position of the line current element in the antenna aperture as defined in [11].

To cover orthogonal polarization planes in the simulation, two antennas with different polarization angles of 90° have to be used. In the next part the scattering behavior of the lap joint caused by the incident field emitted by the two-dimensional antennas is described.

B) Calculation of the target's scattering behavior

A VNA can only measure the scattering parameters of the device under test. Hence, we have to calculate the scattering matrix of the lap joint geometry to compare the CFIE approach to a measurement. The different elements of the simulated scattering matrix

$$S_{kl}(u_x) \sim \int_S \left(-\boldsymbol{E}_k^i \cdot \boldsymbol{J}_l^S\left(\boldsymbol{E}_l^i, \boldsymbol{H}_l^i\right)\right) dS \quad (7)$$

[12] can be derived by using the reciprocity theorem at the center frequency of the radar system. To calculate the matrix entries $S_{kl}(u_x)$, the antennas act as transmitter and/or receiver. In (7), $\boldsymbol{E}_k^i$ refers to the incident field at the surface S of the lap joint geometry caused by the kth receiving antenna. The induced electric surface current density $\boldsymbol{J}_l^S(\boldsymbol{E}_l^i, \boldsymbol{H}_l^i)$ is a function of the incident fields caused by the lth antenna. The incident fields and the surface current density are functions of the radar's position. As a consequence, the scattering matrix is also a function of u_x.

The calculation of $\boldsymbol{J}_l^S$ is realized by using the CFIE, which is solved numerically by the MoM [5]. For the MoM calculation the lap joint is split into patches with a length of $\lambda_c/64$ at the step and $\lambda_c/16$ elsewhere. The variable λ_c refers to the wavelength at the center frequency. The additional use of rectangular subdomain basis functions eases the evaluation of all occurring integrals, compared to other kinds of basis functions.

C) Rotation of the antenna system over the lap joint

In this section, we analyze the influences on the co-polarized (S_{11}, S_{22}) and cross-polarized (S_{12}, S_{21}) scattering parameters for different rotation angles of the antenna system φ_{As} pertaining to the lap joint's orientation. In addition, we point out the ideal rotation angle of the antenna system for the measurements. Figure 2 depicts the rotation angle of the antenna system and the rotation angles of the antennas. For the simulation the center of the antenna system is placed over the lap joint step x_K at an altitude of $z_A = 0.11$ m. In addition, the difference in the polarization angles of the antennas is set to 90° as depicted in Fig. 2. For the simulation a lap joint with a step thickness of $t = 10$ mm is chosen. Besides

https://doi.org/10.1017/S1759078713000329 Published online by Cambridge University Press

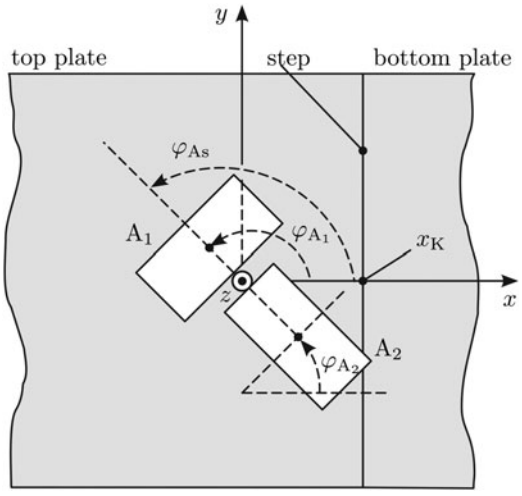

Fig. 2. The sketch shows different angles of the antennas and the antenna system.

that, the simulation is performed at a single frequency namely the center frequency. As discussed in Section II the lap joint step is aligned with the *y*-axis. Now the antennas are rotated around the *z*-axis.

In the two-dimensional simulation, this geometrical rotation can be done mathematically by rotating the polarization of the emitted electromagnetic field of each antenna. During the simulation, the polarization angle of the antenna system φ_{AS} is varied from 0° to 180° (see Fig. 2). Since we have a polarization difference between the two antennas, this implicates a rotation angle $\varphi_{A_1} = 0°$ to 180° for the first and $\varphi_{A_2} = -90°$ to 90° for the second antenna. The resulting magnitudes of the scattering matrix are depicted in Fig. 3. The main finding of this simulation is that the cross-polarized scattering parameter has its maximum magnitude value at $\varphi_{AS} = 45° + n\ 90°$ for $n = \{0, 1, 2, 3\}$. In contrast, the curve shape's maximum of the co-polarized part is $\pm$ 45° shifted compared to the cross-polarized one. The variation in the co-polarized scattering parameters is mainly caused by the thickness of the lap joint. Since we use local polarimetric effects caused by the lap joint, rotation angles of $\varphi_{AS} = 45°$ and $\varphi_{AS} = 135°$ are the ideal choices for continuous simulations and measurements.

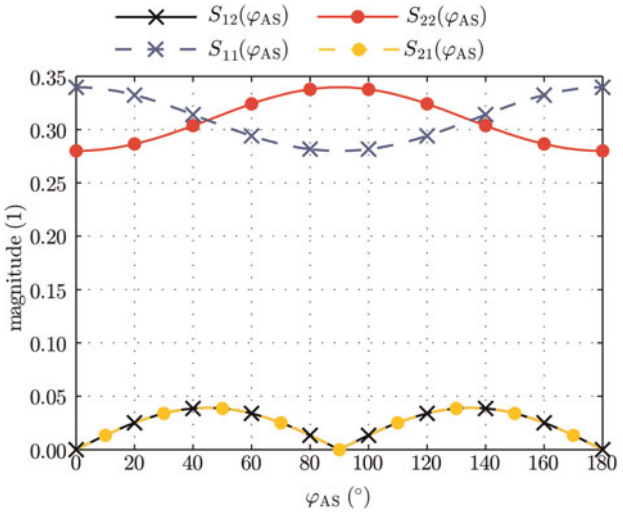

Fig. 3. Simulated scattering parameters for different antenna rotation angles.

IV. VALIDATION OF THE SCATTERING BEHAVIOR

To verify the presented signal model, measurements according to Fig. 1 were conducted. In the measurement we need to gain slant range resolution to separate the lap joint from other targets and annoyances like multi path reflections. This is made possible by performing a frequency sweep from 26.5 to 28.5 GHz with the VNA. This frequency range is chosen because of hardware availability. In contrast to the slant range resolution the cross range resolution is mainly dependent on the synthetic aperture of the system. In contrast to the measurements the CFIE approach is calculated for two dimensions and evaluated at the center frequency only. Hence, additional signal processing tasks have to be conducted before the simulated and measured data can be compared. The comparison between the measurements and the CFIE data is important to analyze the properties of the model reproducing the measured signal.

For the measurements the antennas A_1 and A_2 were connected to port one and two of the VNA, respectively. The scattering matrix was measured for different antenna positions and frequencies. The main diagonal elements correspond to monostatic and co-polarized measurements, and the off-diagonal entries can be interpreted as cross-polarized transmissions from one pyramidal horn antenna to the other, because they are orientated to cover orthogonal polarization planes.

A) Measurements

To conduct measurements, the antenna system is placed at a distance of $z_A = 0.11$ m above the lap joint. The dimensions of the bottom and the top plates are 0.3×0.3 m^2 and 0.15×0.3 m^2, respectively. From measurement to measurement different top plate thicknesses according to $t = \{2, 4, 6, 8, 10, 12\}$ mm are used. The lap joint position is set to $x_K = -13.4$ mm. The properties of the antenna system, the FSCW radar, and the chosen SAR parameters are summarized in Table 1.

Table 1. Measurement setup, FSCW, and SAR parameters

Antenna system		
Antenna gain	G	≈15 dBi
Position of the antenna system	$\mathbf{r}_A$	$[u_x, 0, 0.11]^T$ m
Polarization angle antenna 1	φ_{A_1}	45°
Polarization angle antenna 2	φ_{A_2}	−45°
FSCW (VNA) parameters		
Transmit power	P_t	−2 dBm
Resolution bandwidth	B_{RBW}	10 kHz
Start frequency	f_{start}	26.5 GHz
Stop frequency	f_{stop}	28.5 GHz
Number of frequency points	N	201
SAR parameters		
Synthetic aperture length	L_x	0.1 m
Spatial sampling interval	Δu_x	2 mm
Number of spatial points	M_x	50

https://doi.org/10.1017/S1759078713000329 Published online by Cambridge University Press

The SAR is realized by moving the antenna system along a one-dimensional path as depicted in Fig. 1. At equidistant grid points, measurements have been conducted with the FSCW radar. After finishing the measurement, a two-dimensional data set $X_{kl}(k_r, u_x)$ depending on the antenna positions u_x and the wavenumbers $k_r = 2\pi f/c_0$ at the measured frequencies f, are available. To reduce the data to one dimension, a signal processing work flow, as depicted in Fig. 4, is performed. The reference plane for all VNA measurements is the connector of the horn antennas. When performing measurements it is more convenient to use the aperture plane as reference (as it is done for the simulations). Therefore, the electrical length of the antenna can be interpreted as an additional phase shift between the measurement and the simulation reference plain. The phase shift of the horn antenna can be split into two parts. The first one is caused by the rectangular waveguide of the horn. The second part is defined by the widening of the horn's throat, which can be interpreted as a widening rectangular waveguide. This phase is calculated as described in [13]. The measured data are corrected with respect to this shift for the transmitting and receiving antennas. After that, the frequency-dependent scattering parameters are inverse Fourier transformed for calculating the range profiles of the measured scene. With the range profiles the range value $\hat{r}_{max}$ is calculated according to Fig. 4. Owing to the SAR concept, the distance between the radar and the target rises during the measurements. In the chosen setup (see Table 1) this range variation had an insubstantial influence and is neglected. Hence, the measured signal is only evaluated at $\hat{r}_{max}$, which corresponds to the range containing the dominant reflection of the lap joint. The evaluation at a single bin reduces the two-dimensional measured data to a one-dimensional signal $X_{12,1D}(u_x) = X_{12}(r, u_x)|_{r=\hat{r}_{max}}$ depending on u_x at the center frequency f_c.

Figure 5 depicts the range profile of the measured data and the calculated range $\hat{r}_{max}$. The phase of $X_{12,1D}$ (u_x) only depends on the center frequency and the target's position related to the antenna system. This can be derived by calculating the range profile of a single point target s_p $(k_r, \mathbf{r}_A(u_x))$,

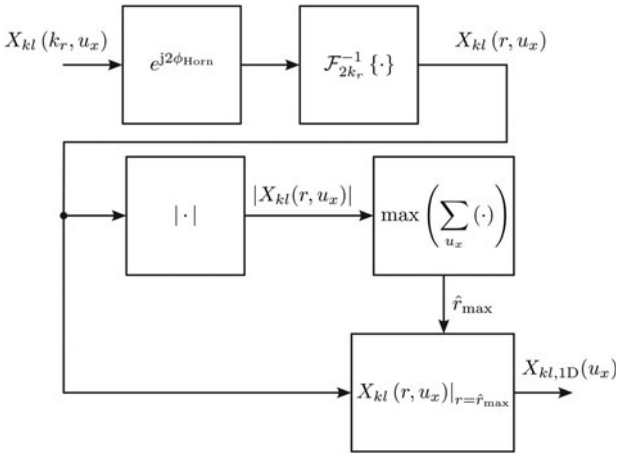

Fig. 4. Block schematic of the signal processing tasks to get a one-dimensional data set from the measurement data.

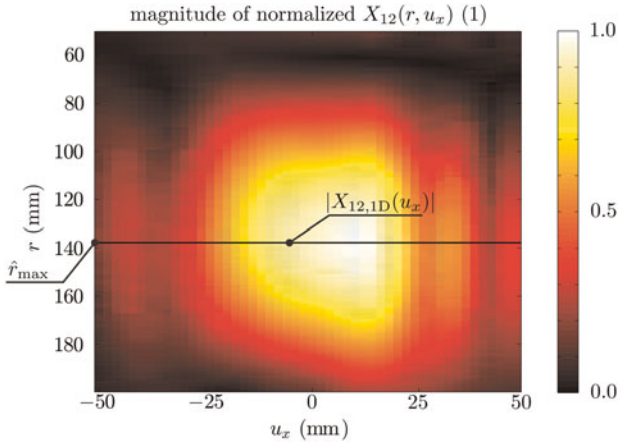

Fig. 5. Magnitude of the measured parameter X_{12} (u_x, r) normalized to its maximum. In addition, we depict the range bin $\hat{r}_{max}$.

which yields

$$S_p(r, u_x) = \int_{k_c-\frac{k_B}{2}}^{k_c+\frac{k_B}{2}} \underbrace{A_p w_A^2\big(\boldsymbol{r}_A(u_x), \boldsymbol{r}_p\big) e^{-j2k_r|r_p - r_A(u_x)|}}_{s_p(k_r, \boldsymbol{r}_A(u_x))} e^{-j2k_r r}\, d2k_r$$

$$= A_p w_A^2\big(\boldsymbol{r}_A(u_x), \boldsymbol{r}_p\big) k_B \mathrm{sinc}\left(\frac{k_B}{2}\big(r - |\boldsymbol{r}_p - \boldsymbol{r}_A(u_x)|\big)\right) \times e^{jk_c(r-|r_p - r_A(u_x)|)}. \quad (8)$$

The signal s_p $(k_r, r_A(u_x))$ depends on the wavenumber k_r as well as the aperture position r_A (u_x). The variable c_0 describes the propagation velocity of the electromagnetic wave. In (8), A_p refers to the complex amplitude of the point target, placed at r_p, and w_A^2 accounts for the radiation characteristic of the antennas. After calculating the inverse Fourier transform with the integration limits $k_c \pm k_B/2$, where $k_B = 2\pi B/c_0$ refers to the wavenumber of the sweep bandwidth B, we get the range profile of the point target. The phase of the outcome in (8) only depends on the position of the target and the center wavenumber k_c. For the position estimation of the lap joint in Section V we use $X_{12,1D}(u_x)$. Therefore, it is adequate to calculate the CFIE approach at the center frequency. The signal $X_{12,1D}$ (u_x) is compared to the simulation results of the CFIE. The real parts of the measurement signals for thicknesses $t =$ 10 mm and $t = 2$ mm and the numerical model calibrated to the amplitude of the measured signal are plotted in Fig. 6. As depicted in Fig. 6, the numerical simulations and the measurements for different thicknesses are in good agreement. This leads to the conclusion that the main scattering effects of the geometry are preserved within the two-dimensional simulation.

V. EDGE ESTIMATION WITH THE NUMERICAL MODEL

The numerical and a point target model are used to estimate the lap joint position. We introduce two types of models for the CFIE approach. For both, it is assumed that the

https://doi.org/10.1017/S1759078713000329 Published online by Cambridge University Press

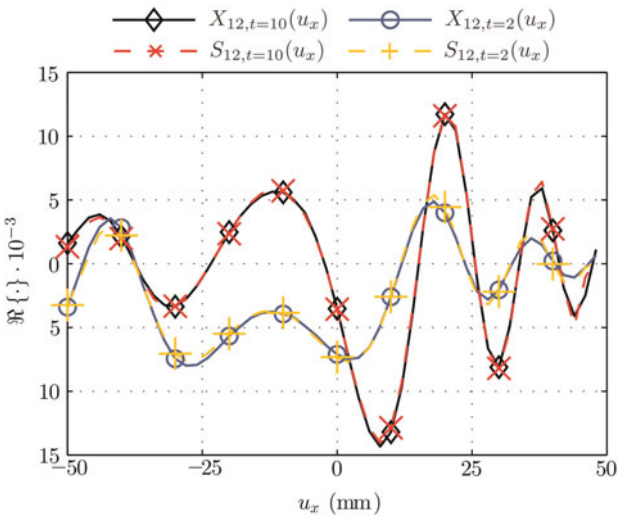

Fig. 6. Real part of the measured parameter $X_{12,\,1D}(u_x)$ and the enhanced numerical model as described in Section V (B) for a one-dimensional aperture along u_x and different thicknesses $t = 10$ mm and $t = 2$ mm.

thickness of the top plate t is known. Therefore, only the position of the lap joint has to be estimated from the measurements.

A) Basic modeling

The SAR measurements are available on an equidistant grid at the positions

$$u_x = m_x \Delta u_x \quad m_x = -\frac{M_x}{2},\ -\frac{M_x}{2}+1,\ \ldots,\ \frac{M_x}{2}-1, \tag{9}$$

where Δu_x denotes the spatial sampling interval and M_x denotes the number of spatial samples. In addition, it is assumed that the measurements are corrupted with complex, additive, white Gaussian noise $w \sim CN(0, \sigma^2)$. Therefore, the data for the position estimation

$$X_{12,1D}[m_x] = Ae^{j\phi_A} S_{12}[m_x] + w[m_x], \tag{10}$$

consists of a sum of the deterministic signal $S_{12}[m_x]$ and the stochastic part $w[m_x]$. The estimation algorithm is based on a least squares approach. For the estimation we identify $\theta = x_K$ as the non-linear and $\tilde{A} = Ae^{j\phi_A}$ as the linear parameter. This approach is known from the literature [14, 15] as the principle of separable least squares. The variable $\tilde{A}$ is used to calibrate the amplitude of the model to the measurements. The vector

$$\boldsymbol{H}(\theta) = \left[S_{12}\left[-\frac{M_x}{2}\right], S_{12}\left[-\frac{M_x}{2}+1\right], \ldots, S_{12}\left[\frac{M_x}{2}-1\right]\right]^T \tag{11}$$

can be defined and only depends on the non-linear parameter $\theta = x_K$. The vector of the data set $\boldsymbol{X}_{12,1D}$ is defined by

$$\boldsymbol{X}_{12,1D} = \left[X_{12,1D}\left[-\frac{M_x}{2}\right], X_{12,1D}\left[-\frac{M_x}{2}+1\right], \ldots, X_{12,1D}\left[\frac{M_x}{2}-1\right]\right]^T. \tag{12}$$

Now we can write the cost function in vector form

$$J(\tilde{A}, \theta) = \left(\boldsymbol{X}_{12,1D} - \boldsymbol{H}(\theta)\tilde{A}\right)^H \left(\boldsymbol{X}_{12,1D} - \boldsymbol{H}(\theta)\tilde{A}\right), \tag{13}$$

which has to be minimized to find the linear and the non-linear parameters. It can be found in the literature [14, 15] that minimizing $J(\tilde{A}, \theta)$ is equal to maximizing

$$J'(\theta) = \boldsymbol{X}_{12,1D}^H \boldsymbol{H}(\theta)\left(\boldsymbol{H}^H(\theta)\boldsymbol{H}(\theta)\right)^{-1}\boldsymbol{H}^H(\theta)\boldsymbol{X}_{12,1D}. \tag{14}$$

After substituting $\boldsymbol{H}(\theta)$ and $\boldsymbol{X}_{12,1D}$ in (14) we get the estimator of the lap joint position

$$\hat{x}_K = \arg\max_{x_K} \left\{ \frac{\sum_{m_x=-\frac{M_x}{2}}^{\frac{M_x}{2}-1} X_{12,1D}^*[m_x] S_{12}[m_x] \sum_{m_x=-\frac{M_x}{2}}^{\frac{M_x}{2}-1} X_{12,1D}[m_x] S_{12}^*[m_x]}{\sum_{m_x=-\frac{M_x}{2}}^{\frac{M_x}{2}-1} S_{12}^*[m_x] S_{12}[m_x]} \right\}, \tag{15}$$

where the $\hat{\cdot}$ denotes $\hat{x}_K$ as an estimated parameter. For the estimation a reference signal is calculated for the known step thickness t with the numerical model described in Section III. The maximization of the cost function (15) and therefore the estimation of the lap joint position can be calculated efficiently in the spectral domain by using the shift property of the Fourier transform. This reduces the computational effort, because the model must be calculated using the CFIE only once. A grid-search algorithm in combination with the Nelder–Mead simplex algorithm [16] is used to maximize $J'(\theta)$.

Figure 7 shows the calculated cost function $J'(\theta)$ for a point target model $J'_{p,t}(\hat{x}_K)$ and the numerical model $J'_{s,t}(\hat{x}_K)$ for lap joint targets with $t = 10$ mm and $t = 2$ mm. The functions were normalized to the maximum of $J'_{s,t=10}(\hat{x}_K)$. The peaks' positions depict the estimated positions $\hat{x}_K$ of the lap joint.

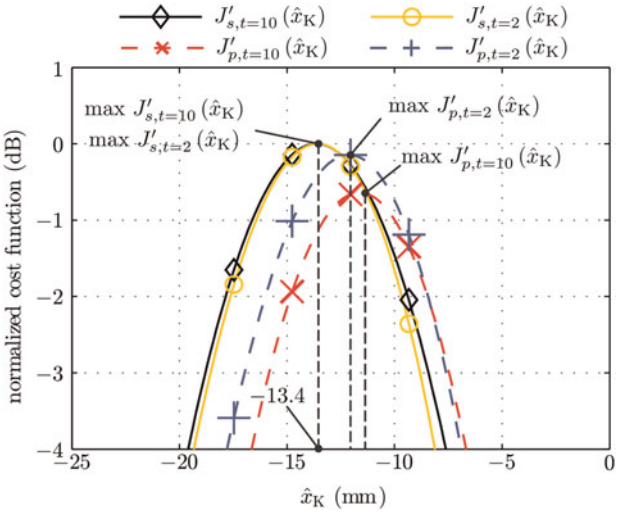

Fig. 7. Cost functions of the numerical and the point target model for the step heights $t = 10$ mm and $t = 2$ mm.

https://doi.org/10.1017/S1759078713000329 Published online by Cambridge University Press

B) Enhanced modeling

During the measurement the gained cross-polarized data is in general corrupted by additional co-polarized parts. These parts are caused by improper alignment of the antennas' polarization planes (φ_{A_1}, φ_{A_2}) and the limited isolation of the antennas between the two polarization planes. In addition, the co-polarized receive power is much higher than the cross-polarized one. To enhance the accuracy of the signal model reproducing the measurements these parts must be taken into account. Therefore, the measured data is expanded with a fraction of the co-polarized scattering parameter, which leads to

$$X_{12,1D}[m_x] = Ae^{j\phi_A} S_{12}[m_x] + Be^{j\phi_B} X_{11,1D,u_0/2}[m_x] + w[m_x]. \tag{16}$$

The complex amplitude $Be^{j\phi_B}$ is used to scale the co-polarized part. The variable $X_{11,1D,u_{0/2}}[m_x]$ refers to the measured co-polarized scattering parameter of the first antenna. Since the center of reference for the bistatic scattering parameters is between the two antennas, the monostatic scattering parameter is shifted about $u_0/2$ related to Fig. 1 to induce $X_{11,1D,u_{0/2}}[m_x]$. Figure 8 shows the real part of the monostatic scattering parameters of antenna A_1, antenna A_2, and the shifted one for a lap joint with $t = 10$ mm. It is also possible to use the simulated parameter $S_{11}[m_x]$ to include non-ideal coupling. Therefore, we have to mention that the co-polarized scattering parameter is sensitive to antenna alignment and meanderings in the lap joint geometry like dents or a tilting of the plates. In contrast to using $X_{11,1D,u_{0/2}}[m_x]$ these unknown influences are also to be estimated when using $S_{11}[m_x]$.

The position estimation is calculated by inserting

$$\boldsymbol{H}(\theta) = \begin{bmatrix} S_{12}\left[-\frac{M_x}{2}\right], S_{12}\left[-\frac{M_x}{2}+1\right], \ldots, S_{12}\left[\frac{M_x}{2}-1\right] \\ X_{11,1D,u_0/2}\left[-\frac{M_x}{2}\right], X_{11,1D,u_0/2}\left[-\frac{M_x}{2}+1\right], \ldots, \\ X_{11,1D,u_0/2}\left[\frac{M_x}{2}-1\right] \end{bmatrix}^T, \tag{17}$$

into (14) and maximizing the cost function, respectively.

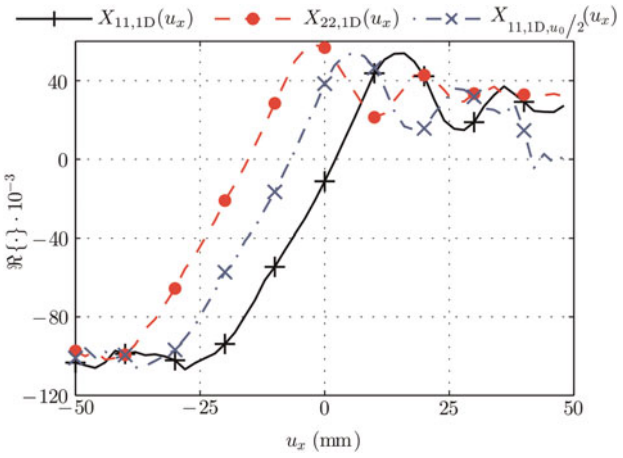

Fig. 8. Real part of the co-polarized and the shifted measurement data.

To prove the achievement of this modeling compared to the basic one, Fig. 9 depicts the errors

$$F_{Bas}(u_x) = \frac{\Re\{\hat{A}e^{j\phi_A} S_{12,\hat{x}_K}(u_x)\} - \Re\{X_{12,1D}(u_x)\}}{\max(\Re\{X_{12,1D}(u_x)\})} 100\% \tag{18}$$

and

$$F_{Enh}(u_x) = \frac{\Re\{\hat{A}e^{j\phi_A} S_{12,\hat{x}_K}(u_x) + \hat{B}e^{j\phi_B} X_{11,1D,u_0/2}(u_x)\} - \Re\{X_{12,1D}(u_x)\}}{\max(\Re\{X_{12,1D}(u_x)\})} 100\% \tag{19}$$

for the basic and the enhanced model for a lap joint with a step thickness $t = 10$ mm. The figure illustrates, that the deviation among the enhanced model and the measurements is much smaller compared to the basic model. This leads to the conclusion, that the corrupting co-polarized parts make an important contribution to the measured data and have to be taken into account to enhance the accuracy of modeling.

The position estimation results of the three analyzed methods (point, basic, and enhanced modeling) for various lap joint thicknesses are summarized in Fig. 10. The outcomes for simulations with the CFIE and measurements with the VNA are depicted. The shown results lead to the conclusion that the estimations realized with the CFIE signal are, in contrast to the point signal, independent of the lap joint's height. Therefore, the point target is not exact enough to describe the scattering behavior of the step as precisely as the CFIE approach. The deviation between the true value and the estimated position is less than half a millimeter for the numerical model for different lap joint thicknesses. Therefore, the two-dimensional CFIE is a better approach to describe the scattering behavior of the step and estimating its position. As a limitation of the CFIE approach we assume, that for small thicknesses t the CFIE approach causes numerical instabilities, since we suggest, that the CFIE and the point target results should agree for small t. Therefore, future investigations

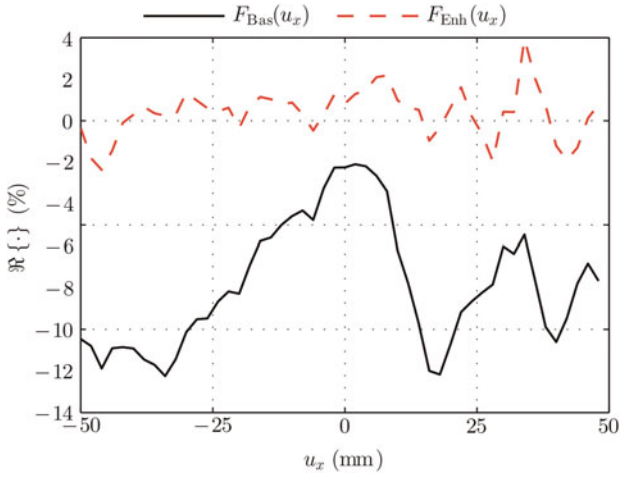

Fig. 9. Real part's relative error related to its maximum between the models and the measurement results.

https://doi.org/10.1017/S1759078713000329 Published online by Cambridge University Press

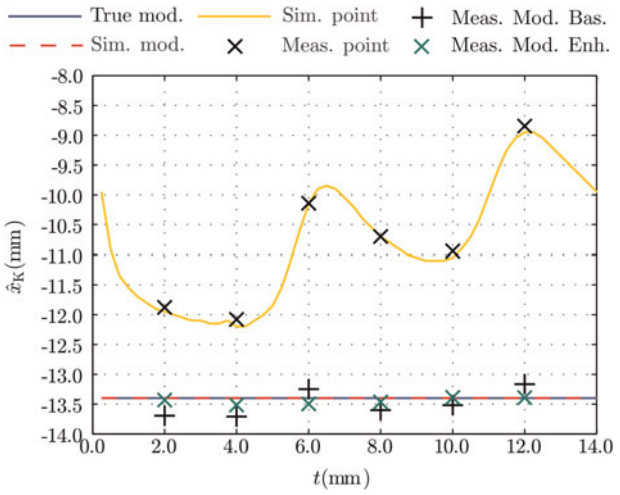

Fig. 10. Estimation results for the point target, the numerical model, and the true position versus the plate thickness.

have to be conducted on the CFIE simulation tool to verify this behavior. Figure 11 shows the relative magnitude of $S_{12,t}(u_x)$ for different thicknesses normalized to the maximum of $S_{11,t=10}(u_x)$. For these simulations the lap joint is placed at $x_K = 0$ mm. The shape of the geometry shifts the peak of $S_{12,t}$ (u_x) and increases the maximum of the received magnitude depending on the ratio between the wavelength and the step's height. This property can be taken as an advantage by facing the antennas toward the step, which will increase the received power. The figure additionally shows the difference in the magnitude from the monostatic and the polarimetric channel. Owing to the monostatic's high magnitude, in contrast to the polarimetric one, crosstalk effects corrupt the polarimetric signal as already discussed in Section B). Therefore, sufficient isolation between the two antennas is required to separate the measured signals. Despite this disadvantage, the polarimetric effects are chosen for position estimation considerations, because they mainly appear in close vicinity to the step of the lap joint in contrast to monostatic scattering.

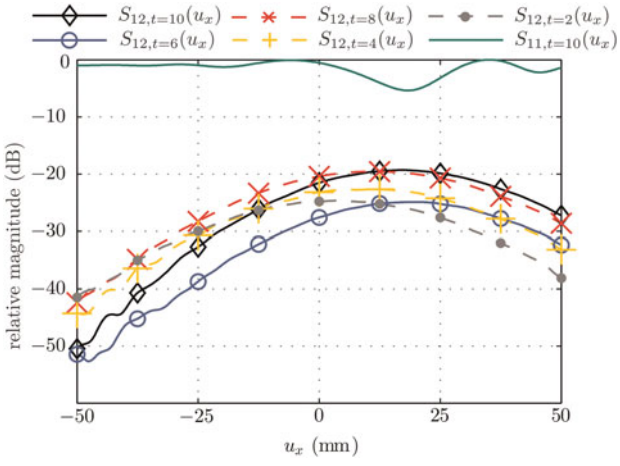

Fig. 11. Relative magnitude of the polarimetric signal model for different edge thicknesses and the monostatic signal for a thickness of 10 mm.

VI. CONCLUSION

We have demonstrated the capabilities of a mm-wave radar system for precise position estimation of lap joints by using polarimetric scattering effects and the concept of a synthetic aperture. For this estimation the efficiency of a point scatterer in comparison to a model based on a CFIE approach is examined. The consideration of additional co-polarized parts in the signal reduces deviation between the measurements and the CFIE model. To reduce the computational costs, the CFIE is calculated for two dimensions and at the center frequency only. In this contribution we highlight that these assumptions have an insubstantial influence on the simulation results. Finally, the study leads to the conclusion, that the robust mm-wave radar systems are well suited to seam tracking tasks in welding applications.

ACKNOWLEDGEMENTS

This work was funded by the COMET/K-project JOIN4+ (825318). The authors express their gratitude to the staff of the Institute for Communications Engineering and RF-Systems for their invaluable technical assistance.

REFERENCES

[1] Michaeli, A.: Equivalent edge currents for arbitrary aspects of observation. IEEE Trans. Antennas Propag., **32** (1984), 252–258.

[2] Balanis, C.A. : Advanced Engineering Electromagnetics, John Wiley & Sons, Inc., New York, 1989.

[3] Ufimtsev, P.Y.: Approximate computation of the diffraction of plane electromagnetic waves at certain metal bodies. Sov. Phys.-Tech. Phys., **55** (1957), 1708–1718.

[4] Knott, E.F.; Senior, T.B.A.: Comparison of three high-frequency diffraction techniques. Proc. IEEE., **62** (1974), 1468–1474.

[5] Harrington, R.F.: Matrix methods for field problems. Proc. IEEE., **55** (1967), 136–149.

[6] Rokhlin, V.: Rapid solution of integral equations of scattering theory in two dimensions. J. Comput. Phys., **86** (1990), 414–439.

[7] Bouché, D.P.; Molinet, F.A.; Mittra, R.: Asymptotic and hybrid techniques for electromagnetic scattering. Proc. IEEE., **81** (1993), 1658–1684.

[8] Mautz, J.R.; Harrington, R.F: H-field, E-field and combined-field solutions for conducting body of revolution. Arch. Elektron. Ubertragungstechn., **32** (1978), 157–164.

[9] Jian-Ming, J.: Theory and Computation of Electromagnetic Fields, IEEE Press and John Wiley & Sons, Inc., New Jersey, 2010.

[10] Balanis, C.A.: Antenna Theory: Analysis and Design, John Wiley & Sons, Inc., New York, 2005.

[11] Joubert, J.; Odendaal, J.W.; Mayhew-Ridgers, G.: On primary incident wave models for pyramidal horn gain calculations. IEEE Trans. Antennas Propag., **48** (2000), 1246–1252.

[12] Haderer, A.; Scherz, P.; Stelzer, A.: Position estimation of thin, conducting plates at mm-wave frequencies utilizing polarimetric effects, in IEEE MTT-S Int. Microwave Symp. Digest 2011, Baltimore, 2011.

[13] Pozar, D.M.: Microwave Engineering, 3rd ed. John Wiley & Sons, Inc., New Jersey, 2005.

https://doi.org/10.1017/S1759078713000329 Published online by Cambridge University Press

[14] Kay, S.M.: Fundamentals of Statistical Signal Processing, vol. I: Estimation Theory, Prentice Hall, Englewood Cliffs Upper Saddle River, NJ, 1993

[15] Golub, G.H.; Pereyra, V.: The differentiation of pseudoinverses and nonlinear least squares problems whose variables separates. SIAM J. Numer. Anal., **10** (1973), 413–432.

[16] Nelder, J.A.; Mead, R.: A simplex method for function minimization. Comput. j., **7** (1965), 308–313.

Jochen O. Schrattenecker was born in Wels, Austria, in 1985. He received the Dipl.-Ing. (M.Sc.) degree in mechatronics from Johannes Kepler University, Linz, Austria in 2011, and is currently working toward the Ph.D. degree at Johannes Kepler University. In 2011, he joined the Institute for Communications Engineering and RF-Systems, Johannes Kepler University, as a Research Assistant. His research topics are radar signal processing, as well as radar system design for industrial sensors.

Andreas Haderer was born in Linz, Austria, in 1980. He received the Dipl.-Ing. (M.Sc.) degree in Electrical Engineering from the Technical University of Graz, Graz, Austria in 2005, and is currently working toward the Ph.D. degree at Johannes Kepler University. In 2005, he joined the Institute for Communications Engineering and RF-Systems, Johannes Kepler University, as an Assistant Professor. His research topics are radar signal processing, as well as synthetic aperture radar systems.

Günther Reinthaler was born in Linz, Austria, in 1977. He received the Dipl.-Ing. (FH) degree in sensor technology and microsystems from FH-Wels (University of Applied Sciences Upper Austria), Austria, Wels, in 2007. In 2007, he started working in the R&D department at Fronius International, Wels. His research work includes the development of sensor systems for automatic welding.

Andreas Stelzer was born in Haslach an der Muhl, Austria, in 1968. He received the Diploma Engineer degree in Electrical Engineering from Technical University of Vienna, Vienna, Austria, in 1994, and the Dr. techn. degree (Ph.D.) in mechatronics (with sub auspiciis praesidentis rei publicae hons.) from Johannes Kepler University, Linz, Austria, in 2000. In 2003, he became Associate Professor with the Institute for Communications Engineering and RF Systems, Johannes Kepler University. Since 2008, he has been a key Researcher for the Austrian Center of Competence in Mechatronics (ACCM), where he is responsible for numerous industrial projects. Since 2007, he has been the head of the Christian Doppler Laboratory for Integrated Radar Sensors, and since 2011 he has been full Professor at Johannes Kepler University, heading the department for RF-Systems. He has authored or coauthored over 280 journal and conference papers. His research is focused on microwave sensor systems for industrial and automotive applications, RF and microwave subsystems, surface acoustic wave (SAW) sensor systems and applications, as well as digital signal processing for sensor signal evaluation.

He is a member of the Austrian ÖVE. He has served as an associate editor for the IEEE Microwave and Wireless Components Letters. He was the recipient of several awards including the 2008 IEEE Microwave Theory and Techniques Society (IEEE MTT-S) Outstanding Young Engineer Award and the 2011 IEEE Microwave Prize. Furthermore, he was recipient of the 2012 European Conference on Antennas and Propagation (EuCAP) Best Measurement Paper Prize, the 2012 Asia Pacific Conference on Antennas and Propagation (APCAP) Best Paper Award, the 2011 German Microwave Conference (GeMiC) Best Paper Award, as well as the EEEfCOM Innovation Award and the European Microwave Association (EuMA) Radar Prize of the European Radar Conference.

https://doi.org/10.1017/S1759078713000329 Published online by Cambridge University Press